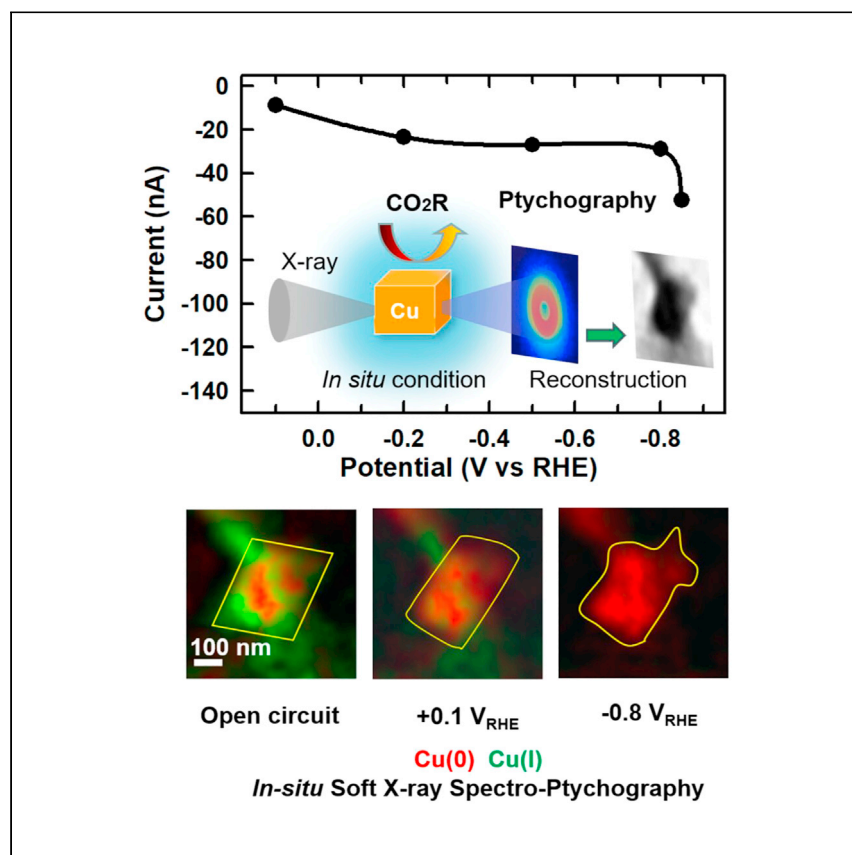


Article

Copper carbon dioxide reduction electrocatalysts studied by *in situ* soft X-ray spectro-ptychography



Zhang et al. report on the morphological and chemical changes of copper electrocatalysts under carbon dioxide reduction conditions using *in situ* soft X-ray spectro-ptychography. Quantitative chemical mapping shows copper particles being reduced to metallic copper and losing their initial cubic structure to form irregular structures during the reaction.

Chunyang Zhang, Nicolas Mille, Haytham Eraky, Stefan Stanescu, Sufal Swaraj, Rachid Belkhou, Drew Higgins, Adam P. Hitchcock

higgid2@mcmaster.ca (D.H.)
aph@mcmaster.ca (A.P.H.)

Highlights

In situ soft X-ray spectro-ptychography is achieved under CO₂ electro-reduction conditions

Spatial resolution is improved via spectro-ptychography compared with *in situ* STXM

Quantitative chemical mapping is provided during reactions

Shape and chemical changes of copper electrocatalysts are studied under reaction conditions

Article

Copper carbon dioxide reduction electrocatalysts studied by *in situ* soft X-ray spectro-ptychography

Chunyang Zhang,^{1,2} Nicolas Mille,³ Haytham Eraky,² Stefan Stanescu,³ Sufal Swaraj,³ Rachid Belkhou,³ Drew Higgins,^{1,4,*} and Adam P. Hitchcock^{2,*}

SUMMARY

Understanding the morphological and chemical structural changes of electrocatalysts under reaction conditions remains a key challenge. Here, we present a detailed study of how individual cubic copper particles change morphology and oxidation state as a function of applied potential during electrochemical carbon dioxide reduction using *in situ* soft X-ray spectro-ptychography. In comparison with scanning transmission X-ray microscopy, the spatial resolution is improved by a factor of 3 through measuring patterns of diffracted photons via spectro-ptychography. Quantitative chemical mapping by *in situ* spectro-ptychography demonstrates that as-deposited, primarily mixed copper (I) and copper (0) particles are completely reduced to pure copper (0) and lose initial cubic structure to form irregular dendritic-like structures. This initial demonstration of *in situ* soft X-ray spectro-ptychography sheds insight on the morphological and chemical changes of copper particles in the carbon dioxide reduction regime and paves the way for more detailed *in situ* studies of electrochemical materials and processes.

INTRODUCTION

Electrochemical carbon dioxide reduction (CO₂R) using renewable electricity offers a sustainable, carbon neutral approach to produce valuable and societally important hydrocarbon, alcohol, and carbonyl products, provided the CO₂ is generated directly from air capture, or from sustainable sources such as biomass combustion, fermentation, or other routes.^{1–3} However, poor energy conversion efficiencies, reaction selectivity, and stability of CO₂R electrocatalysts hinder the large-scale deployment of this process.^{4,5} Among the various electrocatalysts used for CO₂R, copper is the only material that can uniquely convert CO₂ into valuable multi-carbon products (C₂₊), such as ethanol or ethylene, at appreciable rates.^{6–10} Improved understanding of Cu catalysts for electrochemical CO₂ conversion will provide crucial guidance for the development of next-generation, improved performance catalysts and CO₂R device designs. The chemical structures present, and the dynamic morphology of Cu catalysts under reaction conditions, are still under debate.^{11–13} For example, the presence of Cu(I) species or subsurface oxygen during electroreduction has been suggested to improve CO₂R activity and steer the selectivity toward C₂₊ products.^{14–16} Other studies have refuted the presence of significant amounts of partially oxidized Cu species under the electrochemically reducing conditions required for the reaction.^{17–19} Morphological changes also occur in Cu electrocatalysts under CO₂R reaction conditions that will lead to changes in the properties of the catalyst and, by extension, the resultant CO₂R activity and selectivity.^{20,21} This brings into question the suitability of *ex situ* characterization of as-prepared or

¹Chemical Engineering, McMaster University, Hamilton, ON L8S 4M1, Canada

²Chemistry & Chemical Biology, McMaster University, Hamilton, ON L8S 4M1, Canada

³Synchrotron SOLEIL, L'Orme des Merisiers, Departementale 128, 91190 Saint-Aubin, France

⁴Lead contact

*Correspondence: higgid2@mcmaster.ca (D.H.), aph@mcmaster.ca (A.P.H.)

<https://doi.org/10.1016/j.xcrp.2023.101665>

post-CO₂R tested materials for establishing catalyst design principles (i.e., morphological, chemical, or electrochemical properties of a catalyst that engender optimized activity, selectivity, and/or stability). This has motivated the development and implementation of *in situ* characterization methods that enable control of the local reaction conditions and applied electrochemical potentials to gain mechanistic insight into electrochemical CO₂R processes and materials.^{6,22–25} Results from these efforts are crucial for establishing fundamental structure-property-performance relationships that can inform further improvements in Cu-based CO₂R electrocatalyst designs.

Among various *in situ* characterization techniques, spectro-microscopic methods that combine imaging and chemical speciation are particularly useful since they can provide real-time and same-position characterizations to simultaneously monitor changes of oxidation states and morphology under reaction conditions. *In situ* scanning transmission X-ray microscopy (STXM) is a powerful, synchrotron-based, spectro-microscopic technique that provides microscopic imaging alongside spatially resolved quantitative chemical mapping.^{26,27} The chemical sensitivity of the technique is based on near-edge X-ray absorption fine structure (NEXAFS) spectroscopy.²⁸ *In situ* STXM has been used to study charge/discharge processes in battery materials,^{29–31} the electrodeposition of copper,³² and catalysis of oxygen evolution and CO₂R reactions.^{24,33,34} Such studies demonstrate the ability of STXM to provide spatially resolved spectroscopic and microscopic information on the studied materials at different time/potential points during electrochemical processes. However, a major challenge limiting the scientific impact of *in situ* STXM is its limited spatial resolution, typically on the order of 40–50 nm because the size of the focused spot depends on the properties of the zone plate. The challenges of zone plate fabrication are such that it is very difficult to improve the spot size beyond ~20 nm³⁵

Ptychography provides improved spatial resolution in comparison with STXM by measuring coherent X-ray diffraction images (DIs) in transmission at an array of overlapping points on a sample that is not dependent on the X-ray focused spot size.³⁶ A mathematical algorithm is then used to reconstruct the set of DIs into a real space image.^{35–41} Recently, ptychography³⁶ has been implemented in a number of soft X-ray STXM facilities, including the HERMES beamline at Synchrotron SOLEIL,^{37,38} the COSMIC beamline at the Advanced Light Source,^{39,40} the STXM at the Shanghai Synchrotron Radiation Facility,⁴¹ and the spectro-microscopy beamline at the Canadian Light Source.⁴² Ptychography is implemented in an STXM by replacing the post-specimen single-channel detector with an X-ray sensitive camera, for example, the sCMOS camera^{43,44} implemented in the STXM at the HERMES beamline of Synchrotron SOLEIL. For spectro-ptychography, sets of X-ray DI measured with suitable spatial overlap are recorded at a series of photon energies. After suitable reconstruction, the resulting ptychographic amplitude images are converted to ptychography X-ray absorption images (stacks) using the Beer-Lambert law. The resulting ptychographic absorption stacks can then provide spectroscopy-based chemical analyses similar to conventional STXM X-ray absorption stacks, but with an improved spatial resolution that can be sub-10 nm^{39,40}

Ptychography using hard X-rays (>4 keV) is much more developed than ptychography using soft X-rays (<2 keV), in part because X-ray attenuation is not a significant concern and in part because of much longer working distances, alleviating constraints on sample and *in situ* reactor designs.^{39,45–51} On the flip side, soft X-ray microscopy is significantly more challenging due to short focal lengths and thus much less space for *in situ* instrumentation. Despite the challenges, soft X-ray

spectro-microscopy provides unique opportunities to gain insight into electro-catalytic materials and processes due to the higher chemical sensitivity of 3d transition metal L-edge spectroscopy relative to K-shell spectroscopy, along with the potential to spectroscopically image reaction products or intermediate species, using the carbon K-edge, for example.^{37,52} Despite this promise, soft X-rays are prone to attenuation, leading to challenges in the design and implementation of *in situ* soft X-ray spectro-microscopy methods under electrochemical conditions where photons must transmit through reactor walls, an electrolyte layer, and the electro-active materials being characterized. Because of these challenges and the recency of the camera innovations that enable soft X-ray spectro-ptychography,^{43,44} *in situ* soft X-ray spectro-ptychography has not been reported previously, to the best of our knowledge. This situation presents an opportunity for scientific innovation, one that was explicitly flagged in a recent review article.⁴⁵ We note that *in situ* hard X-ray ptychographic imaging of X-ray nucleated, thermally driven growth of Cu₂O particles from a static Cu(acetylacetonitrile)₂ solution was reported recently.⁴⁶ Although oxidation state changes from Cu(I) to Cu(0) in the temporal evolution of the particles was inferred (and verified by non-spatially resolved spectral studies^{53,54}), direct spectroscopy-based, *in situ* evidence of the reduction was not obtained since all measurements were performed at a fixed X-ray energy (15.25 or 8.98 keV). Neither electrochemical processing nor liquid flow was part of that experiment.

In this work, we used *in situ* spectro-ptychography in the soft X-ray region to characterize electro-deposited Cu electrocatalysts under electrochemical CO₂R conditions. By leveraging our custom micro-fluidic reactor design that employs a three-electrode micro-chip electrochemical cell,^{24,32,33} *in situ* soft X-ray spectro-ptychography measurements were conducted under applied electrode potentials in the presence of controlled electrolyte flow. Through direct comparison we demonstrate that the spatial resolution for *in situ* spectro-microscopy measurements is improved 3-fold by using spectro-ptychography rather than conventional STXM. Characterization of Cu electrocatalysts under controlled electrochemical CO₂R conditions enabled us to monitor the morphology and spatially resolved oxidation state changes occurring both within a single Cu particle and multiple Cu particles distributed over a wider region of the electrode surface. The measurements showed that initially electrodeposited Cu(0)/Cu(I)-based particles are converted to metallic Cu at potentials approaching or below -0.2 V versus the reversible hydrogen electrode (V_{RHE}). At more reducing electrode potentials where electrochemical CO₂R occurs, a single Cu particle was observed to undergo morphological changes from a cubic structure to a dendritic-like particle structure. This study demonstrates that *in situ* soft X-ray spectro-ptychography is an effective approach for attaining fundamental insight into the morphology and chemical structures of electro-catalysts under electrochemical CO₂R conditions.

RESULTS

Brief description of techniques and experiments

In situ spectro-ptychography experiments were conducted using a custom-designed microfluidic device encompassing an electrochemical micro-chip reactor (see [experimental procedures](#)). A brief description of the fundamental physics of ptychography is provided in the supplemental information, [Note S1](#), and [Figures S1–S3](#). For more extensive details, examples and discussion of ptychography, readers are referred to citations in [Note S1](#). Cu particles were prepared by electrodeposition on the working electrode from a solution of 0.01 M CuSO₄ and 0.01 M KCl. After electrodeposition, the electrolyte was changed to CO₂-saturated 0.1 M KHCO₃ followed by the application of electrode potential to initiate CO₂R. More details are provided in the

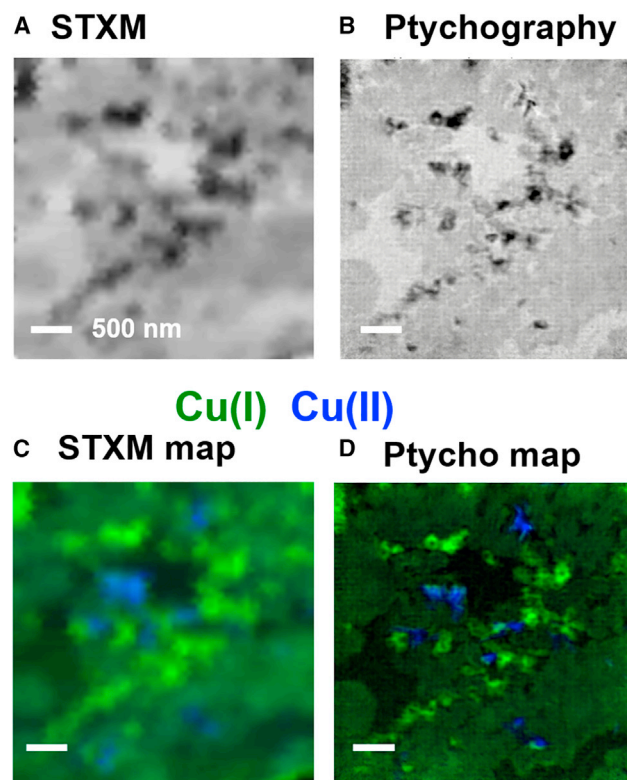


Figure 1. Comparison of imaging and chemical mapping by *in situ* STXM and *in situ* spectro-ptychography of area A

(A) *In situ* STXM transmission image at 933.3 eV.

(B) *In situ* ptychography amplitude image at 933.3 eV. Color-coded composite of Cu(I) (green) and Cu(II) (blue) component maps, derived from (C) the fit of an *in situ* STXM 4-E stack and (D) the fit of an *in situ* spectro-ptychography (Ptycho) 4-E stack. All measurements were collected under open circuit potential (OCP) conditions in CO₂-saturated 0.1 M KHCO₃. Scale bars, 500 nm.

Experimental procedures. The presentation of results in this manuscript is organized as follows. Comparing *in situ* STXM and ptychography (area A) compares the results of *in situ* STXM and *in situ* spectro-ptychography measured on electrodeposited Cu catalyst particles, which we denote as “area A” at open circuit potential (OCP) conditions in CO₂-saturated 0.1 M KHCO₃. *In situ* spectro-ptychography of Cu particles under CO₂R conditions (area B) reports *in situ* spectro-ptychography results for Cu particles on a region of a different electrode surface that was subjected to an applied potential of +0.1 V_{RHE}, which we denote as “area B.” Morphological and chemical changes of a single Cu particle under CO₂R conditions reports spectro-ptychography results from an individual Cu particle while subjecting it to a stepwise series of chrono-amperometry holds between OCP and −0.85 V_{RHE}, which is in the range of electrochemical CO₂R. We denote this Cu particle as “area C.” More details about techniques and experiments are shown in the [experimental procedures](#) and supplemental information.

Comparing *in situ* STXM and ptychography (area A)

Figure 1 compares *in situ* STXM (Figure 1A) and *in situ* ptychography (Figure 1B) images at 933.3 eV (the peak energy of Cu L₃ absorption of Cu metal and Cu₂O) of deposited Cu particles in area A measured at OCP in CO₂-saturated 0.1 M KHCO₃. The Cu particles range in size from ~300 nm to 1 μm, with the particles better resolved in the ptychography image than in the STXM image. As outlined

in [Note S2](#), the spatial resolution of *in situ* ptychography is estimated to be $\sim 25 \pm 5$ nm from a Fourier ring correlation analysis ([Figure S4](#)), which is confirmed by evaluating the abruptness of sharp features in the amplitude images ([Figure S5](#)). This is considerably better than the $\sim 75 \pm 10$ nm spatial resolution of the same features measured from the corresponding *in situ* STXM image. Typically, ptychography can provide up to five times improvement in spatial resolution relative to the resolution determined by using a focused probe and single-channel, integrated signal detection (i.e., STXM). Perhaps more important is that the quality of the ptychography image in terms of signal-to-noise and sampling is much better than that of STXM. This is in part due to a longer acquisition time and in part to a finer pixel size in the reconstructed images. In this work, each diffraction image was integrated for 60 ms and the reconstruction pixel size was 5.5 nm. In contrast, the STXM measurements used 20 ms sampling and 100 nm pixels. Due to the ptychography measurement conditions used—1 μm spot size and 80%–90% overlap—a given sample area contributes to many DI and these in turn contribute to the signal at each 5.5 nm pixel in the reconstructed amplitude image. In addition, the ptychographic reconstruction partly compensates for scanning artifacts in the STXM, which cause smearing of the boundary of particles and thus lower resolution. Another important point is that, with the use of a defocused spot size (1 μm in this study), the radiation dose is much smaller in spectro-ptychography than a corresponding STXM measurement. As discussed in [Note S15](#), the estimated reduction in dose by using ptychography instead of STXM is a factor of 6.

To investigate the chemical identity and quantify the composition of electrodeposited Cu catalyst particles in area A, *in situ* STXM and ptychography images were measured at four photon energies (927.3, 930.3, 933.3, and 937.3 eV), which we denote as a four-energy (4-E) stack. These four photon energy values were selected as they allow an unambiguous differentiation of Cu(0), Cu(I), and Cu(II) oxidation states based on the Cu L_3 X-ray absorption spectra of Cu, Cu_2O , and CuO ([Note S3](#) and [Figure S6](#)).⁵⁵ At each of the four photon energies the contrast of the particles in the STXM and ptychography images changes significantly (see [Note S4](#) and [Figure S7](#)). Analysis with suitable reference spectra⁵⁵ is used to map the different Cu oxidation states present within the particles. Although the reference spectra used in this work were those digitized from Jiang et al.,⁵⁵ we have recently re-measured these spectra in STXM, with identical results and identical analysis outcomes. The average spectrum of the Cu particles from the 4-E STXM stack ([Figure S7c](#)) and 4-E spectro-ptychography stack ([Figure S7d](#)) of area A indicate the presence of both Cu(I) and Cu(II) after electro-deposition. The component maps for Cu(0), Cu(I), and Cu(II) were derived from fitting ([Note S5](#); [Figure S8](#)). [Figure 1C](#) presents a rescaled color-coded composite of the STXM-derived Cu(I) and Cu(II) component maps showing that the particles in area A are mainly Cu(I) or Cu(II). Cu(0) was detected in area A, as shown in [Figure S8](#). To focus on the improvement in spatial resolution afforded by ptychography, we have only included the Cu(I) and Cu(II) signals in the color-coded composites ([Figures 1C](#) and [1D](#)).

Ptychography stack measurements were conducted using the same 4-E approach. The resulting amplitude images ([Figure S7](#)) show contrast variations similar to those in the 4-E STXM images ([Figure S7A](#)) but with higher spatial resolution. The 4-E ptychography stack was analyzed to generate Cu(0), Cu(I), and Cu(II) component maps. [Figure 1D](#) presents a rescaled color-coded composite of the ptychography-derived Cu(I) and Cu(II) component maps. The spatial distributions of Cu(I) and Cu(II) are similar to those derived from STXM, albeit with much higher spatial resolution.

***In situ* spectro-ptychography of Cu particles under CO₂R conditions (area B)**

Another electrodeposited Cu-based electrode (area B) was prepared *in situ*. After changing the electrolyte to CO₂-saturated 0.1 M KHCO₃, a Cu L₃ ptychography stack (40 energies from 920 to 946 eV) was measured at an applied potential of +0.1 V_{RHE}. The chrono-amperometry results (current as a function of time) are presented in Note S6 and Figure S9A. Figure 2 presents the results of analysis of this Cu L₃ spectro-ptychography stack. The stack images were converted to optical densities and fit to quantitative Cu, Cu₂O, and CuO reference spectra (Figure S6) using the singular value decomposition (SVD) matrix method, described in more detail elsewhere.⁵⁶ This forward fitting analysis generates quantitative component maps of each chemical species with amplitudes providing the thickness of each species at each pixel in the area measured. Additional details regarding data processing are provided in Experimental procedures. Quantitative maps of Cu(0), Cu(I), and Cu(II) were derived from the Cu L₃ spectro-ptychography stack (Figures 2C–2E). The particles observed in this region range in size from a few tens of nm to ~300 nm (Figure 2A). In contrast to area A, the particles in area B are mainly Cu(0), with a very small amount of Cu(I). There is also a very small amount of Cu(II) more or less uniformly distributed over the electrode. To check these results, an alternate, multivariate statistical analysis was applied to this dataset, with results presented in Note S10. This analysis reports there are at most three statistically significant spectral components. The first two components are pure metallic Cu and a slightly modified metallic Cu due to mixture with a small signal of Cu(I). These two signals account for over 99% of the variance of the dataset while the third component is attributed to noise.

To further confirm this analysis, the spectra of the Cu(I)- and Cu(0)-rich regions were extracted and analyzed to verify the quantitative composition of each region. These spectral analysis results (Figure S9) are consistent with the mapping analysis. Cu(0) is the largest contributor (>95%), showing that, under +0.1 V_{RHE} *in situ* conditions, the majority of Cu(I) and Cu(II) species (such as those observed at OCP in area A) were reduced into metallic Cu. Figure 2B shows the ptychography amplitude spectra of Cu(0), Cu(I), and Cu(II) derived from the spectro-ptychography data.

In addition to the amplitude signal, which is similar to conventional X-ray absorption, ptychography measurements also provide phase images and thus a phase spectro-microscopy. Figure S10 (Note S7) is a sketch outlining the relationship of X-ray absorption, ptychography amplitude, and ptychography phase signals. Phase spectra are quite different from absorption spectra. It is of interest to see if there is complementary, or perhaps even new, information from phase spectroscopy.⁴⁵ The phase spectra of Cu(0), Cu(I), and Cu(II) (displayed in Figure 3A) were generated by extracting the signal from the phase stack at the spatial locations of Cu(0), Cu(I), and Cu(II) determined by the analysis of the ptychography absorption stack (Figure 2) (i.e., from the same measurement). These phase spectra were used to make an SVD analysis of the Cu L₃ spectro-ptychography phase image stack (Figure 3). The spatial distributions of Cu(0), Cu(I), and Cu(II) components (Figures 3B–3D) and a relative scale color-coded composite (Figure 3F) derived from the phase stack are similar to those derived from the ptychography amplitude stack. The residual of the fit (Figure 3E) is rather featureless at the spatial scale of the particles, but it does contain a slowly varying diagonal structure. We interpret this as a result of changes in the phase of the incident probe over the course of the measurement. The probe phase is assumed to be constant in the ptychographic reconstruction. As with the analysis of the amplitude signal, a small amount of Cu(II) is reported from the fit. The phase signal of Cu(II) is quite sharp and occurs ~2 eV below the Cu(0) and Cu(I) phase

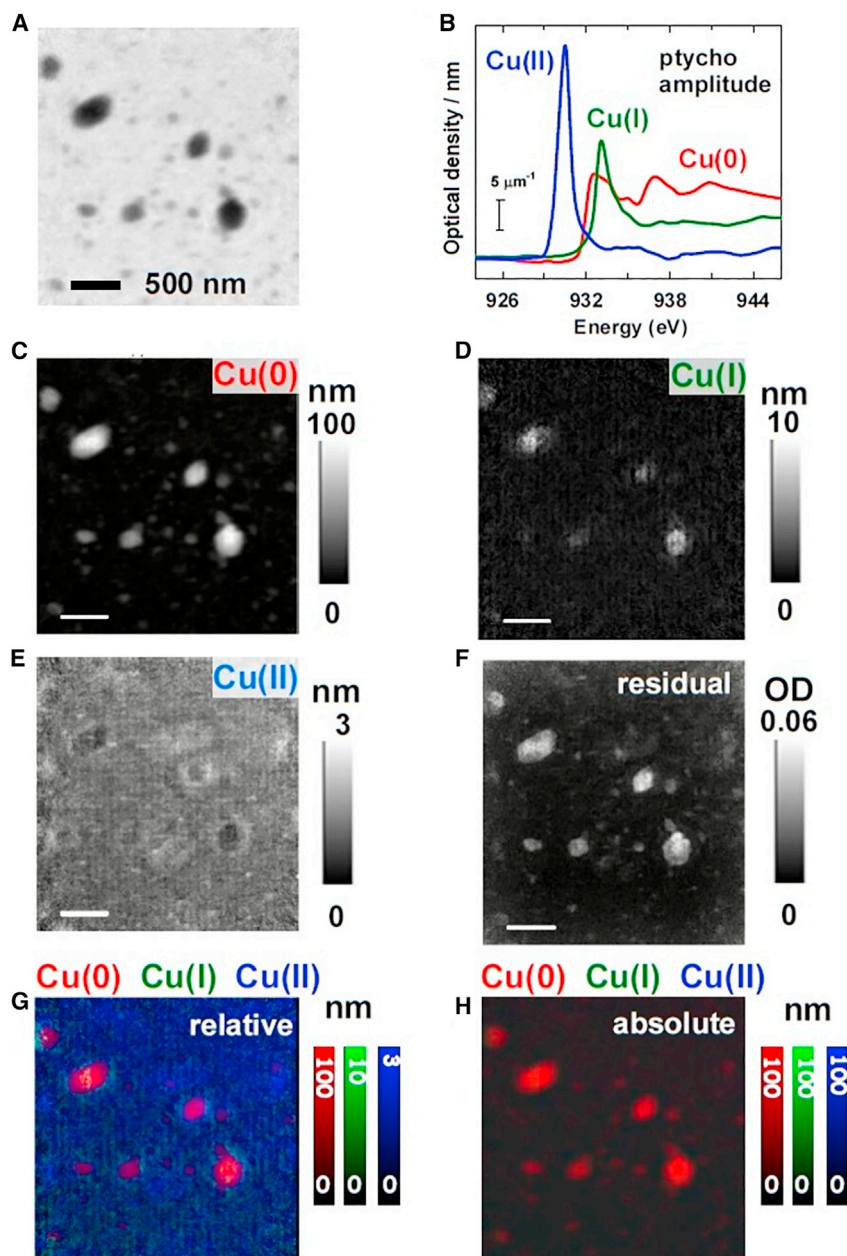


Figure 2. Cu L₃ *in situ* spectro-ptychography analysis of area B at +0.1 V_{RHE}

(A) Ptychography amplitude image at 933.3 eV.

(B–E) (B) Reference spectra of Cu(0), Cu(I), and Cu(II) from *in situ* spectro-ptychography (Ptycho) measurements, indicated by the 5 μm⁻¹ vertical scale bar. Component maps, derived from the fit of the reference spectra to the ptychography amplitude (absorption) stack, for (C) Cu(0), (D) Cu(I), and (E) Cu(II). The intensity scales show the thickness in nm.

(F) Residual of fit.

(G) Color-coded composite of the component maps using relative scaling.

(H) Color-coded component map using absolute scaling. Measurements were conducted in CO₂-saturated 0.1 M KHCO₃. Scale bars, 500 nm.

signals, which means the sensitivity to Cu(II) is very high. The particles consist of Cu(I) and Cu(0), as indicated in the color-coded composites of component maps derived from both the ptychography amplitude (Figure 2G) and ptychography phase

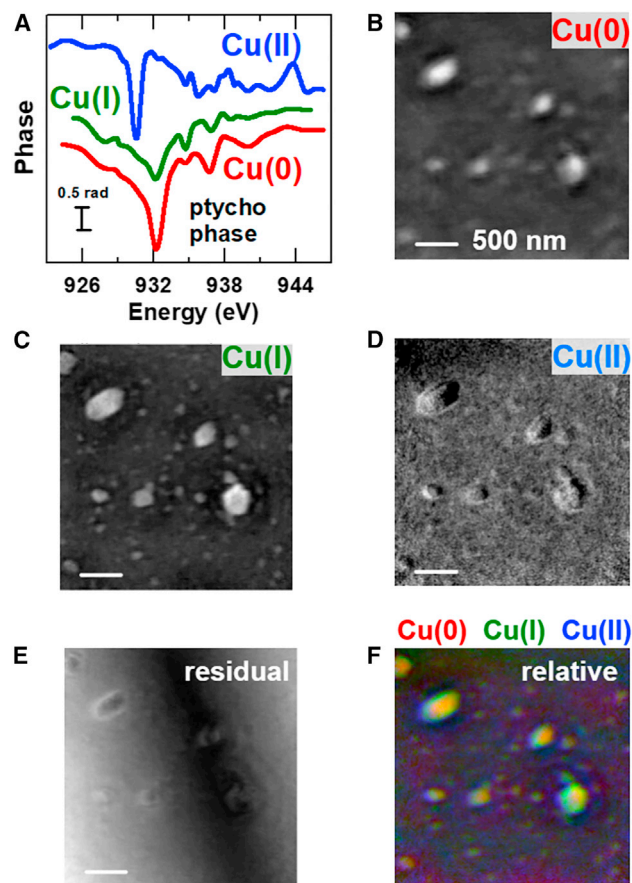


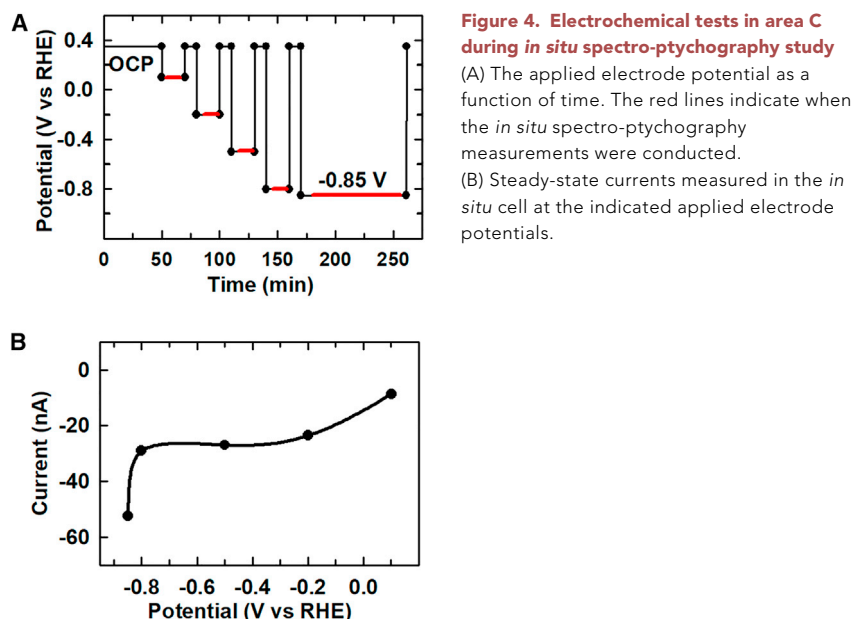
Figure 3. Analysis of full Cu L_3 *in situ* spectro-ptychography phase stack of area B

(A) Reference spectra from *in situ* spectro-ptychography (Ptycho) phase stack.
 (B) Cu metal component map derived from fit of the phase stack using the reference spectra in (A).
 (C) Cu(I) component map from phase.
 (D) Cu(II) component map from phase.
 (E) Residual of fit.
 (F) Color-coded component map using relative scaling. Scale bars, 500 nm.

(Figure 3F) stacks. It is noteworthy that, based only on contrast, the analysis of the phase signals suggests more Cu(I) relative to Cu(0) than determined from the amplitude signals. We think that this does not mean there is more Cu(I); rather just that the phase is more sensitive to Cu(I) than to Cu(0). Basically, at this point in the development of soft X-ray ptychography, the relationship between phase spectra and material thickness is not sufficiently understood so as to allow quantitative analysis of phase signals measured by spectro-ptychography. Thus, there is no intensity scale bar for the component maps displayed in Figure 3.

Morphological and chemical changes of a single Cu particle under CO_2R conditions

In situ spectro-ptychography was used to measure the morphology and spatially resolved oxidation state distributions in a single Cu particle (denoted as area C) in CO_2 -saturated 0.1 M $KHCO_3$ under a series of applied electrode potentials (OCP, +0.1, -0.2, -0.5, -0.8, and -0.85 V_{RHE}) spanning electrochemical CO_2R conditions. After collecting *in situ* spectro-ptychography 4-E stacks or fully sampled Cu L_3 energy stacks at each applied electrode potential, the electrode was returned to OCP ($\sim 0.36 V_{RHE}$) to return to the same catalyst starting state. Figure 4A depicts the



electrode potential profile as a function of time utilized during the sequence of measurements. The steady-state current measured during the chronoamperometry measurement holds are plotted in Figure 4B. Note S8 and Figure S11 display the current as a function of time at each potential. We note that faradic efficiencies, current densities, and product distributions for CO₂R using the same type of electrocatalyst (electrodeposited Cu on Au) were measured in a lab-based two-compartment electrochemical cell.³³ The similarity of the onset of higher negative currents and unambiguous product-based evidence of CO₂ reduction³³ are direct evidence that the larger negative current observed at electrode potentials below $-0.8 V_{\text{RHE}}$ in Figure 4B is due to CO₂R reactions.

Figure 5A displays an STXM transmission image at 933.3 eV of area C. Figure 5B is an expansion in the area of the *in situ* spectro-ptychography studies for a single Cu particle with a pseudo-cubic morphology. Figure 5C shows the ptychography amplitude image at 933.3 eV measured from the same area. The improvement in spatial resolution is dramatic (~ 25 nm in ptychography versus ~ 75 nm in STXM; Figures S5 and S6). The edges of the particle are much better defined in ptychography, allowing us to track changes in the particle morphology as a function of electrode potential under CO₂R conditions. The Cu particle in Figure 5C showed a cubic shape prior to applying potential, very similar to the structure of Cu particles reported in the literature prepared by similar methods.^{9–12,25,57,58}

Ptychography 4-E stacks were used to quantitatively monitor the morphology and chemical changes in the Cu-based particle as a function of potential from +0.1 to $-0.8 V_{\text{RHE}}$. Figures 5D–5G show ptychography amplitude images at 933.3 eV, collected at the four different electrode potentials indicated in the figure. As the electrode potential becomes increasingly negative and enters the regime of CO₂R ($\sim < -0.2$ V versus RHE), the Cu particle loses its initial cubic structure and grows small, sharp dendrites. The reconstructed 4-E ptychography amplitude stacks were converted to absorption and analyzed by SVD fitting to obtain quantitative component maps of each Cu species, as shown in Note S9 and Figure S12. The

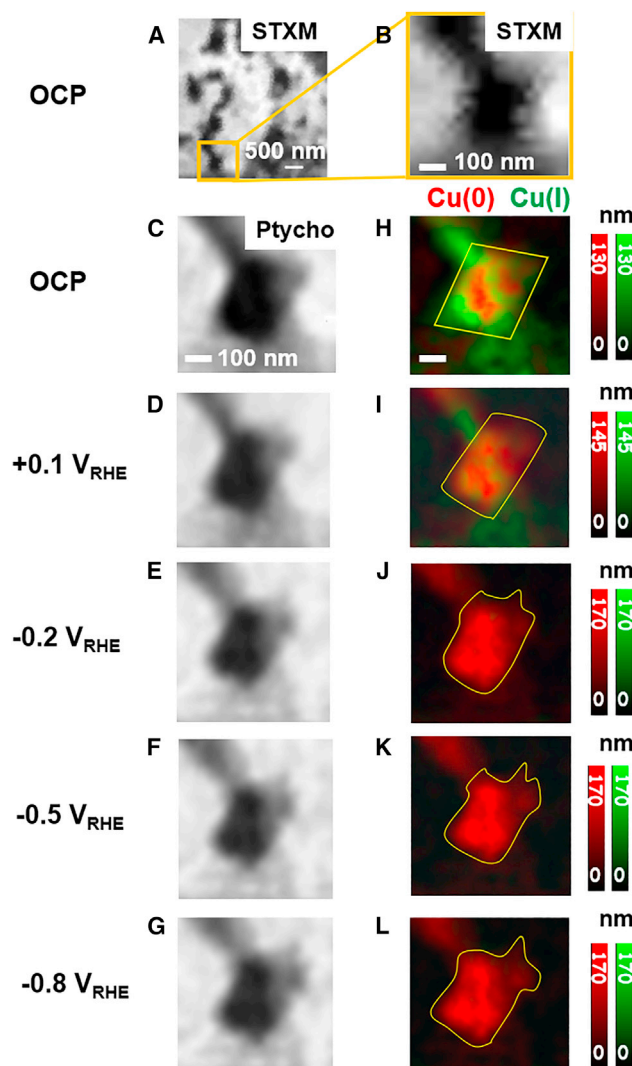


Figure 5. *In situ* spectro-ptychography study of the cubic Cu particle

(A) STXM image of area C at 933.3 eV at OCP and (B) STXM image of the Cu cubic particle at 933.3 eV. Ptychography (Ptycho) amplitude images at 933.3 eV of the Cu cubic particle at (C) OCP, (D) $+0.1 V_{RHE}$, (E) $-0.2 V_{RHE}$, (F) $-0.5 V_{RHE}$, and (G) $-0.8 V_{RHE}$. Color-coded composite of the Cu(0) (red) and Cu(I) (green) component maps of the cubic particle derived from *in situ* spectro-ptychography 4-E stacks measured at (H) OCP, (I) $+0.1 V_{RHE}$, (J) $-0.2 V_{RHE}$, (K) $-0.5 V_{RHE}$, and (L) $-0.8 V_{RHE}$. The yellow contour lines in (H–L) identify the regions with thickness of Cu(0) or Cu(I) higher than 20 nm (see Figure S12). Scale bars, 500 nm (A) and 100 nm (B–L).

color-coded composite component maps of Cu(0), Cu(I), and Cu(II) in absolute scaling (showing the thickness of the materials in units of nm) are presented in Figures 5H–5L, showing the spatially resolved distribution of each Cu species under each electrode potential. At OCP, the cubic particle was a mixture of Cu(0) and Cu(I). When more negative electrode potentials were applied, the Cu(I) in the cubic particle converted to Cu(0), with almost all of the Cu(I) being converted to Cu(0) at potentials below $-0.2 V_{RHE}$.

The average spectrum of the Cu cubic particle (regions of yellow shapes in Figures 5H–5L) extracted from the 4-E and fully sampled Cu L_3 spectro-ptychography amplitude stacks as a function of electrode potential ($+0.1$ to $-0.85 V_{RHE}$) are

Table 1. Compositions of Cu cubic particles under various potentials

Potential (V_{RHE})	Average thickness (nm) ^a		
	Cu(0)	Cu(I)	Cu(II)
OCP	69 ± 5	45 ± 4	<1
+0.1	81 ± 7	19 ± 2	<1
-0.2	83 ± 7	<1	<1
-0.5	76 ± 6	<1	<1
-0.8	78 ± 6	<1	<1
-0.85	60 ± 5	<1	<1

^aThe uncertainties combine statistical ($\pm 3\%$) and estimated systematic uncertainties. The latter were estimated by comparing quantitation of component maps derived from slight but reasonable changes in the analysis procedure.

presented in Figure S13. The evolution of the average spectrum confirms the conversion from Cu(I) to Cu(0) during the electrochemical process. Moreover, the spectra extracted from the Cu(0)-rich and Cu(I)-rich regions were analyzed by SVD using the OD1 (optical density per nm) reference spectra to quantify the composition under various potentials. The results showing the average thickness of each Cu species on the Cu nanoparticles are presented in Table 1. This spectral-domain analysis confirms the changes of Cu oxidation states during the CO₂R reactions. No statistically significant amounts of Cu(I) were detected at potentials more negative than $-0.2 V_{\text{RHE}}$, verifying that Cu(0) is the oxidation state of the active catalyst under electrochemical CO₂R conditions. The average thickness of Cu(0) gradually reducing could be due to the detachment of Cu materials from the catalytic particles during the CO₂R process, which has been observed in other literature.²⁰ Our results quantitatively show the Cu detachment during the reactions.

A detailed Cu L₃ ptychography stack was measured during chronoamperometry at $-0.85 V_{\text{RHE}}$, where Cu is very active for the electrochemical conversion of CO₂ into alcohol and hydrocarbon products.^{33,59} Under these electrochemical conditions, bubbles were occasionally observed at or near the working electrode surface, likely due to the formation of gas-phase CO₂R products (CO, small hydrocarbons) and/or H₂ evolution from water splitting. An example of a spectro-ptychography measurement under gas evolution conditions is presented in Note S11, Figure S16, and Video S1. Despite the changing position of the liquid interface, it was still possible to conduct spectro-ptychography measurements on the same cubic Cu particle. Quantitative component maps of Cu(0), Cu(I), and Cu(II) and a color-coded composite of the component maps from processing of the ptychography amplitude stack are presented in Note S12 and Figure S17. The results from the full spectro-ptychography stack are similar to those from the 4-E stack measured at $-0.8 V_{\text{RHE}}$ (Figures 5L and S13), thereby verifying the chemical analysis provided by the 4-E stack.

DISCUSSION

Individually, *in situ* flow electrochemical STXM and soft X-ray spectro-ptychography are very challenging experimental methods. The combination of controlled *in situ* electrochemical modification of samples in the presence of a liquid electrolyte and soft X-ray spectro-ptychography has not been reported previously in the scientific literature to the best of our knowledge. In this work, we demonstrate the application of *in situ* spectro-ptychography under controlled electrolyte flow and applied electrode potentials to characterize Cu catalysts under electrochemical CO₂R conditions. This research shows that spectro-ptychography can provide chemically selective imaging under *in situ* conditions with results similar to those from STXM, albeit

with superior spatial resolution and image quality. The improved spatial resolution provides increased insight into the morphological changes as the catalyst particles evolve under reducing conditions (Figures 1 and 5). The combination of improved spatial resolution and the ability to quantitatively map Cu oxidation states with high spatial resolution made it possible to monitor the morphological and chemical state evolution of a single Cu particle under CO₂R conditions.

Using *in situ* spectroscopic^{4,6,11,23} or microscopic characterizations,^{10,20} some studies have reported the presence of Cu(I) under electro-catalytic CO₂R conditions,^{3,10,14–17} while others report only Cu(0).^{18–20} The quantitative, spectroscopy-based results from our *in situ* spectro-ptychography measurements provide further insight into this issue. As reported in Table 1, within estimated errors, the particles are 100% ± 7% Cu(0) at electrode potentials of $-0.2 V_{\text{RHE}}$ or lower. This strongly supports the viewpoint that non-zero-valent Cu species do not exist under steady-state electrochemical CO₂R conditions.^{18–20} After complete conversion of Cu(I) to Cu(0) at $-0.2 V_{\text{RHE}}$, there are no further oxidation state changes, but morphology changes continue in the form of dendrite growth (Figure 5). This suggests that Cu particles do not change shape solely as a result of changing oxidation state. Rather the morphology changes are the result of restructuring, reconstruction, and re-deposition processes caused by the driving forces associated with the CO₂R reaction itself.^{20–23,25} These results are in good accord with a sub-set of other *in situ* studies of the same type of Cu CO₂R electrocatalysts.^{3,4,6,20,21,25} In addition, they are supported by the results of a parallel study we have conducted using *in situ* STXM on a similar electrocatalyst using the same *in situ* device and protocol, including electrodeposition from CuSO₄/KCl, followed by changing the electrolyte to CO₂-saturated KHCO₃ and potential dependent chronoamperometry. The *in situ* STXM measurements were made over a larger area of the electrode and thus a much larger number of Cu-based particles. The trends observed in the *in situ* STXM study are consistent with those reported in this work.³³

Overall, this study demonstrates that *in situ* soft X-ray spectro-ptychography provides sensitive and quantitative chemical speciation with high spatial resolution, which gives insight into the complex structural and chemical evolution of CO₂R and other electrocatalysts. In this study we found that *in situ* spectro-ptychography is practical for small areas (<2 μm). Larger areas, with the required large overlap sampling (>80%, see experimental procedures), take too long and can generate datasets larger than the SOLEIL HERMES ptycho processing computers can handle. Currently, the upper limit at HERMES for PyNX analysis of a single ptychography dataset (1 real space image) is 2,500 DI. Thus spectro-ptychography is best suited to studies of detailed changes in small areas. In the context of studies of Cu-based CO₂R electrocatalysis, the 4-E Cu L₃ stack approach is very time efficient, allowing studies of a larger range of *in situ* conditions within a limited time period. We estimate that 4-E stacks save more than 75% of the time compared with 40 energy stacks. This raises the potential of following the kinetics of some changes, as long as the processes occur in the timescale of a few minutes. However, it is always useful to measure the detailed energy stacks at selected conditions, both to confirm results from faster 4-E stacks and to check for unexpected components.

As a final comment, the total elapsed time for spectro-ptychography using defocused spot size (e.g., 1 μm, as used in this work) is not much longer than what would be required to measure STXM of the same area with suitable parameters. Basically the spatial sampling has to be much greater in STXM than in spectro-ptychography to

sufficiently sample the morphology. The data collection time for spectro-ptychography of area B was 90 min. To measure the same area by STXM using a 20 nm spot size and 5 ms/pixel the acquisition time would be 70 min (3×3 , 150×150 pixels, 5 ms/pixel, 34 energies). If the same dwell time as spectro-ptychography was used (60 ms), the time for the analogous STXM measurement would be 14 h. That long an STXM measurement would deliver an enormous radiation dose. So, for the size of areas studied in this work, ptychography has a slight advantage in elapsed time (ignoring the significant amount of time needed for ptychography reconstruction!) and huge advantages in terms of (1) much finer pixels in the final reconstructed images, (2) better spatial resolution, (3) better statistics, and (4) greatly reduced radiation dose, and thus less concern about radiation damage. Aside from the effort and computational resources needed to carry out the reconstruction (which is getting easier year by year), spectro-ptychography has many advantages relative to conventional STXM.

EXPERIMENTAL PROCEDURES

Resource availability

Lead contact

Further information and requests for resources should be directed to, and will be fulfilled, by the lead contact, Drew Higgins (higgid2@mcmaster.ca).

Materials availability

This study did not generate new unique reagents.

Data and code availability

The datasets generated in this study are available from the [lead contact](#) upon reasonable request.

Reagents and chemicals

CuSO_4 , KCl, and KHCO_3 were purchased from Sigma-Aldrich and used as received without further purification. Deionized water was used in all experiments.

In situ device and instrumentation

A custom-designed microfluidic device encompassing an electrochemical microchip reactor³³ was used for these *in situ* studies. The device is presented in more detail in [Note S13](#). The *in situ* device consists of a machined printed circuit board (PCB) ([Figure S18A](#)) front frame, a poly(methyl methacrylate) backplate ([Figure S18B](#)), and a polydimethylsiloxane/glass cell equipped with the electrochemical *in situ* chips ([Figure S18C](#)). The electrode equipped *in situ* chip ([Figure S18D](#)), fabricated by Norcada, is connected to a potentiostat (Ivium pocketstat) through a 4-pin electrical connector on the PCB frame. The four microfluidic channels (shown as dotted lines in [Figure S18C](#)) are connected using Tefzel fluoropolymer tubing (Idex) with an inner diameter of 0.0254 cm and outer diameter of 1.5875 cm. One of these tubes is connected to a syringe pump (New Era 1000) for controlled electrolyte flow. The electrochemical reactions were performed using the three electrodes on base chip E ([Figure S18E](#)). Spacer chip F has a pre-deposited spacer layer (500 nm or 1 μm thick) defining the height of the flow channel. The three electrodes on the base chip E, working/counter/reference electrode (WE/CE/RE), are all gold. ([Figure S18E](#)) The darker circles on the WE and CE are regions with thinner Au coating to reduce X-ray absorption from the electrodes. [Figures S18A](#) and [S18B](#) show pictures of the assembled device inside the HERMES STXM chamber with the Dhyana 92 ptychography camera and associated stray light shield installed.

STXM and ptychography

STXM

The HERMES beamline is described in detail elsewhere.⁶⁰ The STXM is commercial, supplied by RI Research Instruments. The fresnel zone plate (FZP) with an outermost zone width of 25 nm was supplied by Applied Nanotools. The sample was placed on an XYZ piezoelectric stage. The lateral position of the sample relative to the FZP was stabilized to a precision of 5 nm by a differential laser interferometer system.⁶¹ Rectilinear raster scans were used. In STXM mode, the X-rays transmitted through the sample are converted into visible photons by a phosphor and are detected in single-event counting mode by a high-performance photomultiplier tube.

Ptychography

The setup for ptychography and the operating procedures are described in detail elsewhere.^{35,36,39,40} In this work, a modified Dhyana-92 sCMOS camera^{43,44} was used. A coated sensor was used, since X-rays above 900 eV are damaging to the uncoated sensor.⁴³ Before each ptychographic measurement, a statistically precise background was measured with the X-ray beam blocked by an upstream valve. The average background after subtraction of the stable camera background was about 1 electron, giving a dynamic range of over 20,000. A custom holder allows the camera to be mounted on the STXM detector stage with enough positioning flexibility to center the camera on the diffracted image and adjust the sample-to-camera distance as a function of photon energy to ensure fixed- q scans. All ptychography measurements were made using a defocused spot, which reduces radiation dose, due to much lower fluence (factor of 400, relative to the fully focused ~ 50 nm spot). To generate a 1.0 μm defocused spot, the zone plate was moved upstream by 18 μm , a distance calculated from $dr/dz = D/f$ where (dr/dz) is the change in the spot size (dr) for a given change in position of the ZP relative to the sample (dz), D is the diameter of the FZP, and f is the focal length given by $f = D\delta r/E$, where δr is the outermost zone width (25 nm) and E is the photon energy.³⁵ Diffraction images were sampled with 80% or 90% overlap and a 1.0 μm defocused spot.

In situ STXM and ptychography

The WE/CE/RE were gold. All potentials were measured relative to the Au pseudo-reference (V_{Au}) during the experiments. The OCP was $-0.045 \pm 0.01 V_{\text{Au}}$, showing that stable potentials were achieved using the Au pseudo-reference. The measured potentials versus the Au pseudo-reference were subsequently converted to potential versus the RHE (V_{RHE}), by a conversion of $V_{\text{RHE}} = V_{\text{Au}} + 0.4$ V, which was determined by comparing cyclic voltammograms for Cu reduction and oxidation under the *in situ* conditions (versus Au) and under the lab-based conditions (versus RHE), where a Ag/AgCl reference electrode was used to bridge to the RHE scale. The OCP of $-0.045 V_{\text{Au}}$ is equivalent $+0.355 V_{\text{RHE}}$.

Details of the procedures used for the *in situ* measurements are presented in [Note S14](#). First, Cu particles were electrodeposited from a mixture solution of 10 mM CuSO_4 and 10 mM KCl on the thin region of the Au working electrode in the *in situ* device. The electrolyte tubes were pre-filled with CuSO_4/KCl solution and connected with the assembled *in situ* device. Then a syringe pump was used to slowly (50 $\mu\text{L}/\text{h}$) fill the *in situ* device with the electrolyte. The filling process was conducted under an optical microscope (20 \times objective) to confirm that the electrolyte completely fills the window region and that the electrolyte layer is of appropriate thickness, as measured by counting Newton rings. For the first *in situ* experiment, the Cu electrodeposition was carried out by performing three cycles of cyclic voltammetry in the potential range -0.1 to $+0.4 V_{\text{RHE}}$ with a scan rate of 20 mV/s. In this

way, Cu particles were deposited on the WE electrode region, as shown by STXM images in [Figure S19](#). Our goal was to generate cubic particles, as documented using similar, mixed Cu(II) and KCl electrolyte solutions.^{9,10} Copper particles having a well-defined cubic structure have been reported to have good efficiency and C₂₊ selectivity for CO₂ reduction.^{9–12} The changing morphology in these images (all recorded by STXM at 933.3 eV) is caused by electrochemical changes during the *in situ* measurements. The last spectro-ptychography recorded on area A used a fully focused X-ray beam (~50 nm). (The results reported in [Figure 1](#) were measured before that scan.) When the incident flux was increased to >200 MHz by opening the exit slits, the high radiation dose caused X-ray-induced reduction of Cu oxide to copper, as evidenced by the square region observed in area A of the electrode that was illuminated under these high flux conditions (region in yellow square in [Figure S19B](#)). After reducing the incident X-ray flux to that used for this study (20 MHz), radiation damage artifacts were not observed (see [Figures S20](#) and [S21](#)). [Note S15](#) discusses the issue of radiation damage during these measurements in more detail. It estimates the X-ray doses used to obtain the reported results and provides experimental evidence that the results reported in this *in situ* spectro-ptychography study of Cu electrocatalysts were not significantly affected by radiation damage.

After *in situ* Cu deposition under the optical microscopy, the electrolyte was changed to CO₂-saturated 0.1 M KHCO₃ for CO₂R reaction. Millipore Type I Ultrapure water was first used to flush the CuSO₄/KCl out of the *in situ* device. The micro-chip reactor was then filled with CO₂-saturated 0.1 M KHCO₃ electrolyte using the syringe pump with a flow rate of 25 μL/h. The whole process for changing the electrolyte took around 20 min.

Different oxidation states were observed in the particles measured in area A and area B. A possible reason for this is given in supplemental information and [Note S14](#).

After Cu particle deposition and changing the electrolyte to CO₂-saturated 0.1 M KHCO₃, the *in situ* device was carefully loaded into the STXM instrument chamber. Then the air in the chamber tank was replaced with He gas for STXM and spectro-ptychography measurements. In some cases, the tank was pumped to <1 mbar and the tank backfilled with 0.8–1 bar He. In others, a slow flow of He was used to displace the air, without the STXM tank pressure deviating much from 1 bar. Operation at 1 bar greatly reduced the window bulging that is common when operating *in situ* cells with thin silicon nitride (SiN_x) windows. While performing measurements, chronoamperometry at various potentials was applied to the Cu particles on the WE at areas A, B, and C. [Table S2](#) summarizes the potentials and measurements of STXM or spectro-ptychography performed to generate the data presented in this paper. When at low potentials or OCP, an electrolyte flow rate of 20 μL/h was used. While at potentials more negative than $-0.5 V_{\text{RHE}}$, where H₂ and CO gas are produced, a faster electrolyte flow rate (50 μL/h) was applied to remove the gas bubbles from the WE region. Between the measurements and prior to changing the potential, the system was returned to open circuit potential $+0.355 V_{\text{RHE}}$ ($-0.045 V_{\text{Au}}$) in order to have a standard starting point before applying the next potential in sequence.

Ptychography data processing

The basic principles of scanning coherent diffraction imaging, known as ptychography,³⁶ are outlined in [Note S1](#). Spectro-ptychography^{37–39} further extends the basic ptychography imaging method by measuring ptychographic data at a sequence of X-ray energies spanning an X-ray absorption edge of an element of interest, in this

case, the Cu L-edge. Ptychographic reconstruction was carried out using the open-source PyNX software⁶² developed at the European Synchrotron Radiation Facility. Two hundred iterations of the alternate projection algorithm with a single probe function (AP**200) was used for the initial analysis, which could be performed in ~15 m, about the same time it takes to acquire the next spectro-ptychographic 4-E dataset. After the run, the data were re-processed using 800 iterations (AP**800). The increased number of iterations typically reduced the extent of raster grid artifact, and slightly improved spatial resolution. Details of the ptychography acquisition and reconstruction are presented in [Table S2](#).

Spectromicroscopy data processing

Three types of STXM and ptychography measurements were used in this work: image, full stack, 4-E stack. STXM/ptychography images were measured by scanning the sample in a point-by-point mode while recording DI with 20–60 ms acquisition time at each pixel. Spectroscopic information was obtained by recording a stack, which is a series of STXM or ptychography image sequences,⁶³ covering a range of photon energies. In this work, a Cu L₃ stack consisted of measurements at 34 or 40 energies from 920 to 946 eV. A 2 × 2 μm (20 × 20) pixel, 60 ms/DI ptychography stack took ~90 m to measure. When measuring the Cu L₃ STXM stack, using the camera and integrating the full DI, the pixel size was 50–100 nm, with a per pixel dwell of 20 ms, which took ~30 m. The 4-E stack used in this work measured images at 927.3, 930.3, 933.3, and 937.3 eV. This took ~20 m for ptychography and ~15 m for STXM, the 4-E stacks provided similar chemical mapping as a full stack, although the latter gave more complete spectroscopic information.

The STXM and reconstructed ptychography data were analyzed using aXis2000 software.⁶⁴ The images in a stack typically drift by a few hundred nm over a 40–80 eV scan range. Therefore, the stacks were aligned to an ~2 nm registry using a Fourier cross-correlation method. The transmission signal (*I*) of the aligned stack is converted to OD using the Beer Lambert law: $OD_{(x,y)} = -\ln(I/I_0)$, where *I* is the X-ray intensity transmitted through the sample and support, and *I*₀ is the incident X-ray intensity measured off the sample but where the X-rays transmit through all other parts of the X-ray path (optics, windows, zone plate, detector) and the sample support (SiN_x window). After OD conversion, the Cu L₃ X-ray absorption spectra of selected areas (many pixels, which are not necessarily contiguous, but are related by spectroscopy) are extracted from the STXM and ptychography stacks using methods described in greater detail below.

The fitting procedure in aXis2000, which is based on a SVD matrix method,⁵⁶ was used to analyze the stacks. The SVD stack fitting routine fits the NEXAFS spectrum at each pixel to a user-identified set of reference spectra, which can be derived from the spectroscopy on well-defined reference compounds (external). The result of an SVD stack fitting is a set of component maps (spatial distributions), one for each component, along with the residual of the fit.^{26,27} To quantitatively fit the data, reference spectra were converted to an absolute intensity scale, OD1, by scaling the relative intensity spectra so that the signal in the pre-edge and far-continuum (>30 eV above the edge) match the predicted spectrum for the 1 nm thickness of the known composition and density of the reference material, which is calculated using elemental parameters from the Center for X-ray Optics database. The grayscale of the component maps derived from SVD stack fitting using OD1 reference spectra is an estimate of the thickness of that component at each pixel in the region analyzed. To confirm the validity of the spectromicroscopy fitting procedure, spectra are extracted from specific areas of a stack, identified based on morphology

and/or spectral similarity and then subjected to a “curve-fit” procedure in which SVD is used to fit the extracted spectra. When reference spectra on OD1 intensity scales are used in a curve-fit, the contribution of each spectral component is an estimate of the average thickness in nm of that component in the area from which the spectra were extracted. Color-coded composites of the component maps are displayed in both relative and absolute scaling. Relative scaling (e.g., Figure 2G), in which the grayscale values of each component are mapped to a 0–255 bit scale for the color representing that component, shows the locations of a component, independent of the amount of the other components. In contrast, in absolute scaling (e.g., Figure 2H), the thickness values for each component are displayed such that the 0–255 bit scales of the red, green, and blue are each mapped to the same limits, by default, the minimum and maximum of thickness over all three components.

SUPPLEMENTAL INFORMATION

Supplemental information can be found online at <https://doi.org/10.1016/j.xcrp.2023.101665>.

ACKNOWLEDGMENTS

We thank Prof. Martin Obst and his student, Pablo Ingino (Bayreuth University), for sharing the design of their *in situ* cell and assisting with its optimization. We also thank Paul Gatt and Michael Clarke at McMaster University for CNC machining, and Prof. Jose Moran-Mirabal and his students for their assistance with development of the *in situ* spectro-ptychography device. We thank Dr. Hao Yuan for assistance with the FRC analysis. This research was supported by the Natural Sciences and Engineering Research Council of Canada (NSERC) Discovery Grant program, the National Research Council of Canada (NRC) Materials for Clean Fuels Challenge program and TotalEnergies. Measurements were made at the STXM/ptychography end station of the HERMES beamline at Synchrotron SOLEIL. The authors thank synchrotron SOLEIL for the provision of beamtime (proposal no. 20220343).

AUTHOR CONTRIBUTIONS

D.H. and A.P.H. conceived the idea and directed the project. D.H., A.P.H., and C.Z. designed the experiments. C.Z., A.P.H., N.M., S. Stanescu, S. Swaraj, and R.B. carried out the experiments. C.Z. and H.E. contributed to the experimental preparation and instrumental development. C.Z., A.P.H., and D.H., co-wrote the paper. All authors discussed the results and commented on the manuscript.

DECLARATION OF INTERESTS

The authors declare no competing interests.

Received: July 10, 2023

Revised: September 7, 2023

Accepted: October 11, 2023

Published: November 2, 2023

REFERENCES

1. Li, X., Wang, Y., Guan, Y., Wang, J., and Wu, H.B. (2021). Recent advances in metal-based electrocatalysts with hetero-interfaces for CO₂ reduction reaction. *Chem Catal.* **12**, 262–291.
2. Zhang, C., Shahcheraghi, L., Ismail, F., Eraky, H., Yuan, H., Hitchcock, A.P., and Higgins, D. (2022). Chemical Structure and Distribution in Nickel–Nitrogen–Carbon Catalysts for CO₂ Electroreduction Identified by Scanning Transmission X-ray Microscopy. *ACS Catal.* **12**, 8746–8760.
3. Chou, T.C., Chang, C.C., Yu, H.L., Yu, W.Y., Dong, C.L., Velasco-Vélez, J.J., Chuang, C.H., Chen, L.C., Lee, J.F., Chen, J.M., and Wu, H.L. (2020). Controlling the oxidation state of the Cu electrode and reaction intermediates for electrochemical CO₂ reduction to ethylene. *J. Am. Chem. Soc.* **142**, 2857–2867.
4. Gibbons, B.M., Wette, M., Stevens, M.B., Davis, R.C., Siahrostami, S., Kreider, M., Mehta, A., Higgins, D.C., Clemens, B.M., and Jaramillo,

- T.F. (2020). In situ X-ray absorption spectroscopy disentangles the roles of copper and silver in a bimetallic catalyst for the oxygen reduction reaction. *Chem. Mater.* **32**, 1819–1827.
5. De Luna, P., Hahn, C., Higgins, D., Jaffer, S.A., Jaramillo, T.F., and Sargent, E.H. (2019). What would it take for renewably powered electrosynthesis to displace petrochemical processes? *Science* **364**, eaav3506.
6. Yang, Y., Peng, Y., Chen, K., Wei, Y., Li, B., Liu, F., and Yang, P. (2022). Operando Resonant Soft X-ray Scattering Studies of Chemical Environment and Interparticle Dynamics of Cu Nanocatalysts for CO₂ Electroreduction. *Surg. Endosc.* **36**, 8927–8934.
7. Tabassum, H., Yang, X., Zou, R., and Wu, G. (2022). Surface engineering of Cu catalysts for electrochemical reduction of CO₂ to value-added multi-carbon products. *Chem Catal.* **2**, 1561–1593.
8. Hahn, C., Hatsukade, T., Kim, Y.G., Vailionis, A., Baricuauro, J.H., Higgins, D.C., Nitopi, S.A., Soriaga, M.P., and Jaramillo, T.F. (2017). Engineering Cu surfaces for the electrocatalytic conversion of CO₂: Controlling selectivity toward oxygenates and hydrocarbons. *Proc. Natl. Acad. Sci. USA* **114**, 5918–5923.
9. Timoshenko, J., Bergmann, A., Rettenmaier, C., Herzog, A., Arán-Ais, R.M., Jeon, H.S., Haase, F.T., Hejral, U., Grosse, P., Kühn, S., et al. (2022). Steering the structure and selectivity of CO₂ electroreduction catalysts by potential pulses. *Nat. Catal.* **5**, 259–267.
10. Arán-Ais, R.M., Scholten, F., Kunze, S., Rizo, R., and Roldan Cuenya, B. (2020). The role of in situ generated morphological motifs and Cu (I) species in C₂₊ product selectivity during CO₂ pulsed electroreduction. *Nat. Energy* **5**, 317–325.
11. Timoshenko, J., and Roldan Cuenya, B. (2021). In situ/operando electrocatalyst characterization by X-ray absorption spectroscopy. *Chem. Rev.* **121**, 882–961.
12. Nitopi, S., Bertheussen, E., Scott, S.B., Liu, X., Engstfeld, A.K., Horch, S., Seger, B., Stephens, I.E.L., Chan, K., Hahn, C., and Chorkendorff, I. (2019). Progress and perspectives of electrochemical CO₂ reduction on copper in aqueous electrolyte. *Chem. Rev.* **119**, 7610–7672.
13. Kibria, M.G., Edwards, J.P., Gabardo, C.M., Dinh, C.T., Seifitokaldani, A., Sinton, D., and Sargent, E.H. (2019). Electrochemical CO₂ reduction into chemical feedstocks: from mechanistic electrocatalysis models to system design. *Adv. Mater.* **31**, 1807166.
14. Cheng, D., Zhao, Z.J., Zhang, G., Yang, P., Li, L., Gao, H., Liu, S., Chang, X., Chen, S., Wang, T., and Gong, J. (2021). The nature of active sites for carbon dioxide electroreduction over oxide-derived copper catalysts. *Nat. Commun.* **12**, 395.
15. Eilert, A., Cavalca, F., Roberts, F.S., Osterwalder, J., Liu, C., Favaro, M., Crumlin, E.J., Ogasawara, H., Friebe, D., Pettersson, L.G.M., and Nilsson, A. (2017). Subsurface oxygen in oxide-derived copper electrocatalysts for carbon dioxide reduction. *J. Phys. Chem. Lett.* **8**, 285–290.
16. Wang, H.Y., Soldemo, M., Degerman, D., Lömkær, P., Schlueter, C., Nilsson, A., and Amann, P. (2022). Direct Evidence of Subsurface Oxygen Formation in Oxide-Derived Cu by X-ray Photoelectron Spectroscopy. *Angew. Chem., Int. Ed. Engl.* **61**, e202111021.
17. Fields, M., Hong, X., Nørskov, J.K., and Chan, K. (2018). Role of subsurface oxygen on Cu surfaces for CO₂ electrochemical reduction. *J. Phys. Chem. C* **122**, 16209–16215.
18. Scott, S.B., Hogg, T.V., Landers, A.T., Maagaard, T., Bertheussen, E., Lin, J.C., Davis, R.C., Beeman, J.W., Higgins, D., Drisdell, W.S., and Chorkendorff, I. (2019). Absence of oxidized phases in Cu under CO reduction conditions. *ACS Energy Lett.* **4**, 803–804.
19. Lum, Y., and Ager, J.W. (2018). Stability of residual oxides in oxide-derived copper catalysts for electrochemical CO₂ reduction investigated with 18O labeling. *Angew. Chem., Int. Ed. Engl.* **57**, 551–554.
20. Grosse, P., Yoon, A., Rettenmaier, C., Herzog, A., Chee, S.W., and Roldan Cuenya, B. (2021). Dynamic transformation of cubic copper catalysts during CO₂ electroreduction and its impact on catalytic selectivity. *Nat. Commun.* **12**, 6736.
21. Arán-Ais, R.M., Rizo, R., Grosse, P., Algara-Siller, G., Dembélé, K., Plodinec, M., Lunkenbein, T., Chee, S.W., and Cuenya, B.R. (2020). Imaging electrochemically synthesized Cu₂O cubes and their morphological evolution under conditions relevant to CO₂ electroreduction. *Nat. Commun.* **11**, 3489.
22. Alnough, W., Black, R., and Higgins, D. (2021). Judicious selection, validation, and use of reference electrodes for in situ and operando electrocatalysis studies. *Chem Catal.* **1**, 997–1013.
23. Velasco-Velez, J.J., Mom, R.V., Sandoval-Diaz, L.E., Felling, L.J., Chuang, C.H., Gao, D., Jones, T.E., Zhu, Q., Arrigo, R., Roldan Cuenya, B., et al. (2020). Revealing the active phase of copper during the electroreduction of CO₂ in aqueous electrolyte by correlating in situ X-ray spectroscopy and in situ electron microscopy. *ACS Energy Lett.* **5**, 2106–2111.
24. Hitchcock, A.P., Zhang, C., Eraky, H., Shahcheraghi, L., Ismail, F., and Higgins, D. (2021). In situ and Operando Studies with Soft X-Ray Transmission Spectromicroscopy. *Microsc. Microanal.* **27**, 59–60.
25. Yang, Y., Zheng, S., Chu, H., Du, C., Chen, M., Emran, M.Y., Chen, J., Yang, F., Tian, L., and Yang, P. (2023). Operando studies reveal active Cu nanograins for CO₂ electroreduction. *Nature* **15**, 262–269.
26. Ade, H., and Hitchcock, A.P. (2008). NEXAFS microscopy and resonant scattering: Composition and orientation probed in real and reciprocal space. *Polymer* **49**, 643–675.
27. Hitchcock, A.P. (2012). In *Soft X-ray Imaging and Spectromicroscopy* Chapter 22 in Volume II of the Handbook on Nanoscopy, G. Van Tendeloo, D. Van Dyck, and S.J. Pennycook, eds. (Wiley), pp. 745–791.
28. Stöhr, J. (2013). *NEXAFS Spectroscopy*, 25 (Springer Science & Business Media).
29. Nelson Weker, J., and Toney, M.F. (2015). Emerging In Situ and Operando Nanoscale X-Ray Imaging Techniques for Energy Storage Materials. *Adv. Funct. Mater.* **25**, 1622–1637.
30. Lim, J., Li, Y., Alsem, D.H., So, H., Lee, S.C., Bai, P., Cogswell, D.A., Liu, X., Jin, N., Yu, Y.S., and Chueh, W.C. (2016). Origin and hysteresis of lithium compositional spatio-dynamics within battery primary particles. *Science* **353**, 566–571.
31. Chourasia, A.K., Pathak, A.D., Bongu, C., Manikandan, K., Praneeth, S., Naik, K.M., and Sharma, C.S. (2022). In Situ/Operando Characterization Techniques: The Guiding Tool for the Development of Li–CO₂ Battery. *Small Methods* **6**, 2200930.
32. Prabu, V., Obst, M., Hosseinkhannazer, H., Reynolds, M., Rosendahl, S., Wang, J., and Hitchcock, A.P. (2018). Instrumentation for in situ flow electrochemical scanning transmission X-ray microscopy (STXM). *Rev. Sci. Instrum.* **89**, 063702.
33. Zhang, C., Eraky, H., Tan, S., Hitchcock, A.P., and Higgins, D. (2023). In-situ studies of copper-based CO₂ reduction electrocatalysts by scanning transmission soft X-ray microscopy. *ACS Nano*. <https://doi.org/10.1021/acsnano.3c05964>.
34. Mefford, J.T., Akbashev, A.R., Kang, M., Bentley, C.L., Gent, W.E., Deng, H.D., Alsem, D.H., Yu, Y.S., Salmon, N.J., Shapiro, D.A., and Chueh, W.C. (2021). Correlative operando microscopy of oxygen evolution electrocatalysts. *Nature* **593**, 67–73.
35. Jacobsen, C. (2019). *X-Ray Microscopy* (Cambridge University Press).
36. Pfeiffer, F. (2018). X-ray ptychography. *Nat. Photonics* **12**, 9–17.
37. Mille, N., Yuan, H., Vijayakumar, J., Stanescu, S., Swaraj, S., Desjardins, K., Favre-Nicolin, V., Belkhou, R., and Hitchcock, A.P. (2022). Ptychography at the carbon K-edge. *Commun. Mater.* **3**, 8.
38. Vijayakumar, J., Yuan, H., Mille, N., Stanescu, S., Swaraj, S., Favre-Nicolin, V., Najafi, E., Hitchcock, A.P., and Belkhou, R. (2023). Soft X-ray spectro-ptychography of boron nitride nanobamboos, carbon nanotubes and permalloy nanorods. *J. Synchrotron Radiat.* **30**, 746–757.
39. Shapiro, D.A., Yu, Y.S., Tyliczszak, T., Cabana, J., Celestre, R., Chao, W., Kaznatcheev, K., Kilcoyne, A.L.D., Maia, F., Marchesini, S., and Padmore, H.A. (2014). Chemical composition mapping with nanometre resolution by soft X-ray microscopy. *Nat. Photonics* **8**, 765–769.
40. Shapiro, D.A., Babin, S., Celestre, R.S., Chao, W., Conley, R.P., Denes, P., Enders, B., Enfedaque, P., James, S., Joseph, J.M., and Zhao, J. (2020). An ultrahigh-resolution soft x-ray microscope for quantitative analysis of chemically heterogeneous nanomaterials. *Sci. Adv.* **6**, eabc4904.
41. Xu, Z., Wang, C., Liu, H., Tao, X., and Tai, R. (2017, June). Low-dose, high-resolution and high-efficiency ptychography at STXM beamline of SSRF Journal of Physics: Conference Series. IOP Publishing 849 (No. 1), 012033.

42. Xia, X., Wang, J., Hu, Y., Liu, J., Darma, A.I., Jin, L., Han, H., He, C., and Yang, J. (2022). Molecular insights into roles of dissolved organic matter in Cr (III) immobilization by coprecipitation with Fe (III) probed by STXM-Ptychography and XANES spectroscopy. *Environ. Sci. Technol.* **56**, 2432–2442.
43. Desjardins, K., Popescu, H., Mercère, P., Meneglier, C., Gaudemer, R., Thânell, K., and Jaouen, N. (2019, January). Characterization of a back-illuminated CMOS camera for soft x-ray coherent scattering. *AIP Conference Proceedings, 2054* (AIP Publishing LLC), 060066. No. 1.
44. Desjardins, K., Medjoubi, K., Sacchi, M., Popescu, H., Gaudemer, R., Belkhou, R., Stanescu, S., Swaraj, S., Besson, A., Vijayakumar, J., and Jaouen, N. (2020). Backside-illuminated scientific CMOS detector for soft X-ray resonant scattering and ptychography. *J. Synchrotron Radiat.* **27**, 1577–1589.
45. Urquhart, S.G. (2022). X-ray Spectroptychography. *ACS Omega* **7**, 11521–11529.
46. Grote, L., Seyrich, M., Döhrmann, R., Harouna-Mayer, S.Y., Mancini, F., Kaziukenas, E., Fernandez-Cuesta, I., A Zito, C., Vasylieva, O., Wittwer, F., and Koziej, D. (2022). Imaging Cu₂O nanocube hollowing in solution by quantitative *in situ* X-ray ptychography. *Nat. Commun.* **13**, 4971.
47. Thibault, P., Dierolf, M., Menzel, A., Bunk, O., David, C., and Pfeiffer, F. (2008). High-resolution scanning x-ray diffraction microscopy. *Science* **321**, 379–382.
48. Fam, Y., Sheppard, T.L., Becher, J., Scherhafer, D., Lambach, H., Kulkarni, S., Keller, T.F., Wittstock, A., Wittwer, F., Seyrich, M., and Grunwaldt, J.D. (2019). A versatile nanoreactor for complementary *in situ* X-ray and electron microscopy studies in catalysis and materials science. *J. Synchrotron Radiat.* **26**, 1769–1781.
49. Hoppe, R., Reinhardt, J., Hofmann, G., Patommel, J., Grunwaldt, J.D., Damsgaard, C.D., Wellenreuther, G., Falkenberg, G., and Schroer, C.G. (2013). High-resolution chemical imaging of gold nanoparticles using hard x-ray ptychography. *Appl. Phys. Lett.* **102**.
50. Baier, S., Damsgaard, C.D., Klumpp, M., Reinhardt, J., Sheppard, T., Balogh, Z., Kasama, T., Benzi, F., Wagner, J.B., Schwieger, W., and Grunwaldt, J.D. (2017). Stability of a bifunctional Cu-based core@zeolite shell catalyst for dimethyl ether synthesis under redox conditions studied by environmental transmission electron microscopy and *in situ* X-ray ptychography. *Microsc. Microanal.* **23**, 501–512.
51. Sun, T., Sun, G., Yu, F., Mao, Y., Tai, R., Zhang, X., Shao, G., Wang, Z., Wang, J., and Zhou, J. (2021). Soft X-ray ptychography chemical imaging of degradation in a composite surface-reconstructed Li-rich cathode. *ACS Nano* **15**, 1475–1485.
52. Wise, A.M., Weker, J.N., Kalirai, S., Farmand, M., Shapiro, D.A., Meirer, F., and Weckhuysen, B.M. (2016). Nanoscale chemical imaging of an individual catalyst particle with soft X-ray ptychography. *ACS Catal.* **6**, 2178–2181.
53. Kränzlin, N., van Beek, W., Niederberger, M., and Koziej, D. (2015). Mechanistic Studies as a Tool for the Design of Copper-Based Heterostructures. *Adv. Mater. Interfac.* **2**, 1500094.
54. Kvashnina, K.O., Butorin, S.M., Modin, A., Soroka, I., Marcellini, M., Guo, J.H., Werme, L., and Nordgren, J. (2007). Changes in electronic structure of copper films in aqueous solutions. *J. Phys. Condens. Matter* **19**, 226002.
55. Jiang, P., Prendergast, D., Borondics, F., Porsgaard, S., Giovanetti, L., Pach, E., Newberg, J., Bluhm, H., Besenbacher, F., and Salmeron, M. (2013). Experimental and theoretical investigation of the electronic structure of Cu₂O and CuO thin films on Cu (110) using x-ray photoelectron and absorption spectroscopy. *J. Chem. Phys.* **138**, 024704.
56. Koprinarov, I.N., Hitchcock, A.P., McCrory, C.T., and Childs, R.F. (2002). Quantitative mapping of structured polymeric systems using singular value decomposition analysis of soft X-ray images. *J. Phys. Chem. B* **106**, 5358–5364.
57. Roberts, F.S., Kuhl, K.P., and Nilsson, A. (2015). High selectivity for ethylene from carbon dioxide reduction over copper nanocube electrocatalysts. *Angew. Chem.* **54**, 5179–5182.
58. Roberts, F.S., Kuhl, K.P., and Nilsson, A. (2016). Electroreduction of carbon monoxide over a copper nanocube catalyst: surface structure and pH dependence on selectivity. *ChemCatChem* **8**, 1119–1124.
59. Higgins, D., Landers, A.T., Ji, Y., Nitopi, S., Morales-Guio, C.G., Wang, L., Chan, K., Hahn, C., and Jaramillo, T.F. (2018). Guiding electrochemical carbon dioxide reduction toward carbonyls using copper silver thin films with interphase miscibility. *ACS Energy Lett.* **3**, 2947–2955.
60. Belkhou, R., Stanescu, S., Swaraj, S., Besson, A., Ledoux, M., Hajlaoui, M., and Dalle, D. (2015). HERMES: a soft X-ray beamline dedicated to X-ray microscopy. *J. Synchrotron Radiat.* **22**, 968–979.
61. Kilcoyne, A.L.D., Tyliszczak, T., Steele, W.F., Fakra, S., Hitchcock, P., Franck, K., Anderson, E., Harteneck, B., Rightor, E.G., Mitchell, G.E., and Ade, H. (2003). Interferometer-controlled scanning transmission X-ray microscopes at the Advanced Light Source. *J. Synchrotron Radiat.* **10**, 125–136.
62. Favre-Nicolin, V., Girard, G., Leake, S., Carnis, J., Chushkin, Y., Kieffer, J., Paleo, P., and Richard, M.I. (2020). PyNX: high-performance computing toolkit for coherent X-ray imaging based on operators. *J. Appl. Crystallogr.* **53**, 1404–1413.
63. Jacobsen, C., Wirick, S., Flynn, G., and Zimba, C. (2000). Soft X-ray spectroscopy from image sequences with sub-100 nm spatial resolution. *J. Microsc.* **197**, 173–184.
64. Hitchcock, A.P. (2023). Analysis of X-ray Images and Spectra (aXis2000): a toolkit for the analysis of X-ray spectromicroscopy data. *J. Electron. Spectrosc. Relat. Phenom.* **266**, 147360.